PHYSICAL REVIEW A **111**, 043526 (2025)

Modulating a photonic graphene lattice by the Lorentz-like transformation

Zhuo Zhang (张卓),[1] Milivoj R. Belić,[2] Yongdong Li (李永东),[1] Tao Wang (王涛),[3] and Yiqi Zhang (张贻齐)[1,4,*]

[1] *Key Laboratory for Physical Electronics and Devices, Ministry of Education, School of Electronic Science and Engineering, Xi'an Jiaotong University, Xi'an, Shaanxi 710049, China*
[2] *College of Science and Engineering, Hamad Bin Khalifa University, 23874 Doha, Qatar*
[3] *Grace Laser, Beijing 101318, China*
[4] *Shaanxi Key Laboratory of Information Photonic Technique, School of Electronic Science and Engineering, Xi'an Jiaotong University, Xi'an, Shaanxi 710049, China*

(Received 16 January 2025; accepted 3 April 2025; published 18 April 2025)

Photonic lattice modulations, such as lattice distortions achieved by stress-strain engineering, have been crucial for the development of various fields of photonics, in particular, topological photonics. Here we modulate the Hermitian and non-Hermitian photonic graphene lattices by utilizing a Lorentz-like transformation applied to the lattice sites. The modulated lattice may fall into two categories, according to the symmetry axis of the lattice. If the axis is aligned in the diagonal direction through the unit cells, the lattice belongs to case II; otherwise, it belongs to case I. For the case-I transformed lattice, the Dirac cones always disappear from the band structure, whereas for the case-II transformed lattice, the Dirac cones only disappear if the transformation angle θ is larger than that of the regular lattice, $\theta = \pi/2$. The Lorentz-like transformation always helps to restore the parity-time ($\mathcal{PT}$) symmetry in the non-Hermitian case-I photonic graphene lattices. In the case II of transformed non-Hermitian lattices, the $\mathcal{PT}$ symmetry can be restored as well, but only for $\theta > \pi/2$. When $\theta < \pi/2$, one obtains exceptional lines in the band structure of the lattice. These results demonstrate that the Lorentz-like transformation can serve as an effective tool to modulate photonic lattices and thus may inspire novel ideas in the manipulation of photonic topological insulators.

DOI: 10.1103/PhysRevA.111.043526

I. INTRODUCTION

Photonic lattice modulation is vital for topological photonics, for various reasons [1–6]. For example, it is there when the inversion symmetry [7–10] or the time-reversal symmetry [11–18] of the lattice needs to be broken, or when one introduces the Kekulé distortion to the lattice [19–24], to fold the Brillouin zone. The modulation enables the strained lattice to produce gauge fields and generate Landau levels [25,26] and novel zero-energy states [27] or restore the parity-time ($\mathcal{PT}$) symmetry [28]. However, the present modulation methods are mostly about the depth of sites, the separation between sites, or the location of sites. Indeed, these modulations did bring many fruitful achievements. Nevertheless, we wonder if there is a method that can modulate the whole lattice at once, without much strain engineering? This topic is meaningful and worth exploring because it may bring about surprising phenomena, promote further development of topological photonics and non-Hermitian physics [29–31], and facilitate potential on-chip applications. Such a method is suggested in this work, and it is surprisingly simple: It explores the lattice modulation by utilizing a Lorentz-like transformation to adjust the lattice coordinates.

As the first step in the special relativity theory, the Lorentz transformation [32] was important for understanding the relativity of simultaneity. In the Minkowski diagram, which elucidates the fact that space and time possess different properties for different observers, the Lorentz transformation helped determine the coordinates of a moving body. The Minkowski diagram is four dimensional and non-Euclidean, hence visualizing it in the real four-dimensional space is not an easy task. In fact, we do not use the Minkowski diagram as such, but only the Lorentz transformation to modulate the two-dimensional lattice coordinates in the Euclidean space. In reality, the transformation is Lorentz like; however, for convenience, we continue to use the term Lorentz transformation in the following text.

The result is shown in Fig. 1, where the horizontal axis is simply x and the vertical axis is y. The angle θ serves as a controlling parameter, as depicted in Fig. 1. In Fig. 1(a) the square space with $\theta = \pi/2$ represents the original configuration, before transformation. The orange rhombus in Fig. 1(b) shows the space after the Lorentz transformation for $\theta = \pi/3$. It is important to note that the diagram in Fig. 1 is entirely two dimensional and Euclidean. As mentioned above, we simply used the Lorentz transformation as a tool to record the modulated coordinates of the photonic lattice. Consequently, we could also select $\theta = 2\pi/3$ for the Lorentz transformation, as shown by the green rhombus in Fig. 1(c).

II. RESULTS

A. Lorentz-transformed lattice

What is clearly demonstrated in Fig. 1 is that the Lorentz transformation can be effectively used to stretch and deform

---

[*] Contact author: zhangyiqi@xjtu.edu.cn

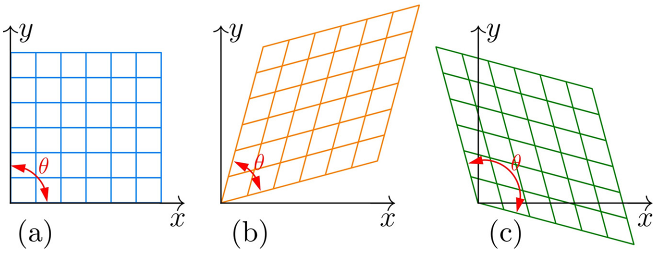

FIG. 1. Minkowski-like diagrams with (a) $\theta = \pi/2$, (b) $\pi/3$, and (c) $2\pi/3$.

the whole lattice at once. We introduce the Lorentz transformation [32] to the lattice through

$$[x' \;\; y']^{\mathrm{T}} = \mathcal{M}[x \;\; y]^{\mathrm{T}}, \tag{1}$$

where the superscript T represents the transposition and the matrix $\mathcal{M}$,

$$\mathcal{M} = \begin{bmatrix} \cosh(\zeta) & -\sinh(\zeta) \\ -\sinh(\zeta) & \cosh(\zeta) \end{bmatrix}, \tag{2}$$

with $\zeta = -1/2\tanh^{-1}(\cos\theta)$, affects the transformation [33,34]. In this way, the lattice undergoes a Lorentz deformation. Obviously, when $\theta = \pi/2$, the lattice remains undeformed, as the matrix $\mathcal{M}$ is then an identity. Since the lattice is controlled by the angle θ, we denote the transformed lattice by $\mathcal{R}(x, y, \theta)$.

In Fig. 2 we present the transformed photonic graphene lattice. The top panel in Fig. 2(a) shows the regular photonic graphene lattice before transformation, with the yellow rhombic region representing the unit cell. The two black edge arrows indicate the basic vectors of the Bravais lattice, while the red dashed line shows the $x = y$ direction, with $\theta = \pi/2$. The lattice after transformation is displayed in the bottom panel of Fig. 2(a), with $\theta = \pi/3$. The unit cell is also deformed, and the lengths of the two basic vectors are now unequal.

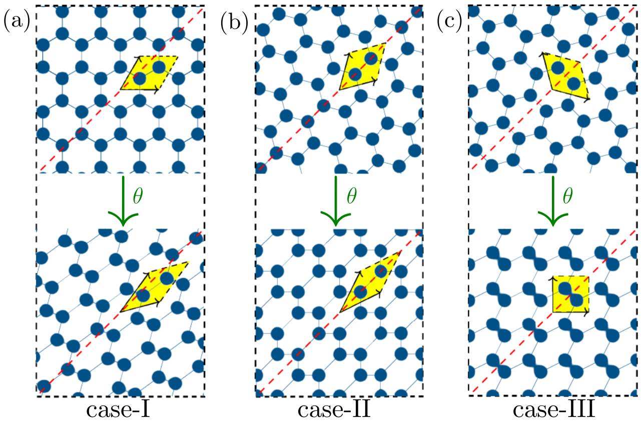

FIG. 2. (a) Shown on top is the regular photonic graphene lattice and on the bottom the transformed photonic graphene lattice from the top, with the controlling parameter θ. (b) Counterclockwise rotated lattice by $\pi/12$ (top) and its transformed counterpart (bottom). (c) Counterclockwise rotated lattice by $\pi/4$ (top) and its transformed counterpart (bottom). The dashed arrow represents the $x = y$ direction and the dashed rhombus filled in yellow is the unit cell.

To avoid such an unnatural situation, one can rotate the regular photonic graphene lattice counterclockwise by $\pi/12$, to align the symmetry axis of the unit cell with the diagonal direction, as shown in the top panel of Fig. 2(b). After the transformation with $\theta = \pi/3$, this lattice is exhibited in the bottom panel of Fig. 2(b). One may note that the two basic vectors have the same length. One could remedy the situation also by rotating the undeformed photonic graphene lattice in Fig. 2(a) counterclockwise by $\pi/4$ and properly choosing the unit cell, as shown in the top panel of Fig. 2(c); the two basic vectors after transformation also have the same length [see the bottom panel in Fig. 2(c)].

For convenience, we refer to the transformations shown in Figs. 2(a), 2(b), and 2(c) as cases I, II, and III, respectively. However, cases II and III are essentially the same, as they are mirror images of each other. In other words, the same transformed lattice is obtained as case II with angle θ and as case III with angle $\pi - \theta$. Therefore, we focus our discussion on the first two cases only.

B. Brillouin zone of the transformed lattice

The Brillouin zone is extremely important in describing the excitation spectrum of waves in periodic media. Due to the transformation, the symmetry of the lattice also changes. Therefore, it is essential to explore the Brillouin zone of the transformed lattice.

In the photonic graphene lattice and its transformed counterparts, there are two primitive lattice vectors $\boldsymbol{a}_i$ that can be chosen on purpose. If we label the primitive vectors of the transformed lattice as $\boldsymbol{a}'_i$, we obtain the relation $\boldsymbol{a}'_i = \mathcal{M}\boldsymbol{a}_i$. Quite generally, one can think of the reciprocal lattice as being a Fourier transform of the direct lattice. According to the reciprocal lattice equation, the primitive lattice vectors $\boldsymbol{b}_i$ in reciprocal space can be obtained analytically. Eventually, we can find the locations of the six corners $\mathbf{K}_i$ of the first Brillouin zone. We have easily identified

$$\begin{aligned} \boldsymbol{a}_1 &= \frac{a}{2}(\sqrt{3}, 3), \\ \boldsymbol{a}_2 &= a(\sqrt{3}, 0), \\ \boldsymbol{a}_3 &= \frac{a}{2}(\sqrt{3}, -3), \end{aligned}$$

where a is the lattice constant, as shown in Fig. 3(a). We should note that only two of the three vectors are independent; the third one can be represented by the first two as $\boldsymbol{a}_3 = \boldsymbol{a}_2 - \boldsymbol{a}_1$. Even though only two vectors are sufficient, we still use all three vectors, for better presentation of the unit cell in the real space and the Brillouin zone in the inverted space. With the degree of transformation $\theta = \pi/3$ in case I, for instance, the primitive vectors of the transformed lattice with $\theta = \pi/3$ are

$$\begin{aligned} \boldsymbol{a}'_1 &= \frac{a}{2\sqrt[4]{3}}(2\sqrt{3}, 3 + \sqrt{3}), \\ \boldsymbol{a}'_2 &= \frac{a}{2\sqrt[4]{3}}(3 + \sqrt{3}, 3 - \sqrt{3}), \\ \boldsymbol{a}'_3 &= \frac{a}{2\sqrt[4]{3}}(3 - \sqrt{3}, -2\sqrt{3}) \end{aligned}$$

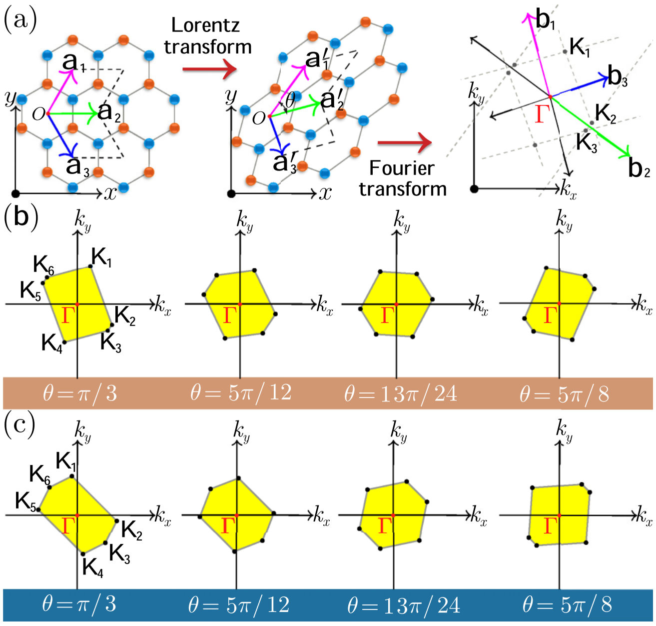

FIG. 3. (a) Lorentz transformation of the lattice with O representing the original point in real space. The view of the lattice in the inverted space is also shown, with Γ the center of the first Brillouin zone. Also shown is the Brillouin zone of the lattice with different θ for (b) case I and (c) case II.

and the corresponding vectors in the inverted space are

$$\boldsymbol{b}_1 = \frac{2\pi}{3\sqrt[4]{3}a}(1-\sqrt{3}, 1+\sqrt{3}),$$
$$\boldsymbol{b}_2 = \frac{2\pi}{3\sqrt[4]{3}a}(1+\sqrt{3}, -2),$$
$$\boldsymbol{b}_3 = \frac{2\pi}{3\sqrt[4]{3}a}(2, \sqrt{3}-1).$$

The locations of the first Brillouin zone can be obtained theoretically as

$$\mathbf{K}_1 = \frac{\pi}{9\sqrt[4]{3}a}(5-\sqrt{3}, 1+5\sqrt{3}),$$
$$\mathbf{K}_2 = \frac{\pi}{9\sqrt[4]{3}a}(7+\sqrt{3}, \sqrt{3}-7),$$
$$\mathbf{K}_3 = \frac{\pi}{9\sqrt[4]{3}a}(1-5\sqrt{3}, 5+\sqrt{3}),$$

which are in accordance with the numerical results in Fig. 3(a). As concerns case II, we just need to take a rotation matrix into account for the Lorentz transformation, so we will not write the vectors explicitly here.

In Figs. 3(b) and 3(c) we illustrate the change in the first Brillouin zone with the transformation angle θ, as highlighted by the yellow regions. The corresponding animations are also produced, to record the changing Brillouin zone with θ [35]. Given various diagrams in Fig. 3 of the Brillouin zone, the role of Lorentz transformation can be better understood, in changing the symmetry of the lattice.

C. Band structure of the transformed lattice

In the following we show how the deformation may help restore the $\mathcal{PT}$ symmetry, based on the continuous model, which includes the shape, depth, and separation of sites in the calculation. As a result, our results will get closer to the real experimental results. First of all, we introduce the governing equation describing the propagation dynamics of a light beam, i.e., the normalized Schrödinger-like paraxial wave equation [11,18,23,24,36,37]

$$i\frac{\partial\psi}{\partial z} = -\frac{1}{2}\nabla_\perp^2\psi - \mathcal{R}(x,y,\theta)\psi, \tag{3}$$

where $\nabla_\perp^2 = \partial_x^2 + \partial_y^2$ is the transverse Laplacian, x and y are the spatial coordinates normalized to r_0, the characteristic transverse scale, and z is the propagation distance normalized to the diffraction length kr_0^2. Here $k = 2n_0\pi/\lambda$ is the wave number, n_0 is the ambient refractive index, and λ is the wavelength. The lattice potential includes the real part $\mathcal{R}_{\rm re}$ and the imaginary part $\mathcal{R}_{\rm im}$, which can be expressed in terms of Gaussian functions [18,23,24,36,38]

$$\mathcal{R}_{\rm re,im} = p_{\rm re,im}\sum_{m,n}\exp\left(-\frac{(\boldsymbol{r}-\boldsymbol{r}_{m,n,\theta})^2}{d^2}\right),$$

with $\boldsymbol{r}(m,n,\theta) = (x_{m,n,\theta}, y_{m,n,\theta})$ the grid coordinates of the lattice and d the width of the waveguide. At this point we give the typical values of the quantities coming from real experiments, based on the femtosecond laser direct writing technique [6,11,18,23,24,36,39]: $\lambda = 800$ nm, $r_0 = 10$ μm, $n_0 = 1.45$, the refractive index change approximately equal to 1.1×10^{-4} for $p_{\rm re} = 1$, and the propagation distance approximately equal to 1 mm for $z = 1$.

The general solution of Eq. (3) can be written in the form $\psi(x,y,z) = u(x,y)\exp(ibz)$, with b the propagation constant, and plugging this solution into Eq. (3), we obtain the eigenvalue problem

$$bu = \tfrac{1}{2}\nabla_\perp^2 u + [\mathcal{R}_{\rm re}(x,y,\theta) + i\mathcal{R}_{\rm im}(x,y,\theta)]u,$$

which can be solved by the plane-wave expansion method [40–42]. In general, the analytical solution of this eigenvalue problem does not exist. Based on this steady-state solution, one forms the band structure of the lattice, which consists in the dependence of the propagation constant b on the transverse wave vector components k_x and k_y of the Bloch waves. Note that here the propagation constant may have both real and imaginary parts, since the lattice potential also features real and imaginary parts.

Having the transformation method at hand, we start our modulation analysis by considering the Hermitian photonic graphene lattice first. Figure 4 shows the band structure (bottom panels) of the Lorentz-transformed modulated photonic graphene (top panels). The top and corresponding bottom panels go together. When $\theta = \pi/2$, the unmodulated band structure shown in Fig. 4(a) displays six Dirac cones, as seen in the bottom panel. For the case-I transformation, the Dirac cones disappear and a band gap forms between the upper and lower bands, if the transformation angle deviates from $\theta = \pi/2$; see the results for $\theta = \pi/3$ and $2\pi/3$ in Fig. 4(b). While for the case-II transformation the Dirac cones disappear only when $\theta > \pi/2$ [cf. the result with $\theta = 2\pi/3$ in Fig. 4(c)],

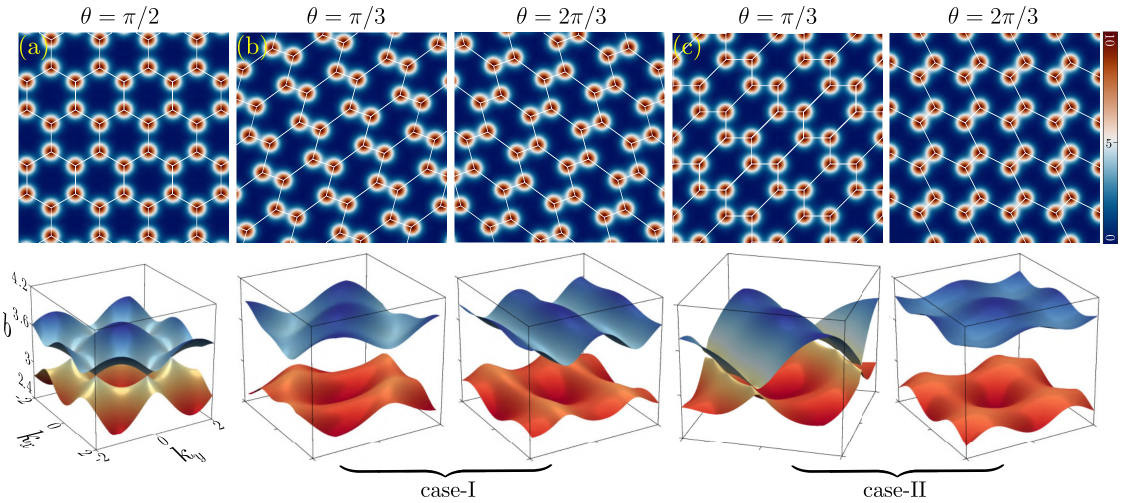

FIG. 4. (a) Band structure (bottom) of the regular photonic graphene lattice (top), with $p_{\rm im} = 0$ and $\theta = \pi/2$. (b) Band structures (bottom) of the case-I photonic graphene lattices (top), with $p_{\rm im} = 0$ and for different θ. (c) Same as in (b) but for case II. The other parameters are $p_{\rm re} = 10$, $d = 0.5$, and lattice constant $a = 1.6$. Red dots in the top row represent the lattice sites

they remain preserved in the region $\theta < \pi/2$ [cf. the result with $\theta = \pi/3$ in Fig. 4(c)].

One can observe that Dirac cones are greatly deformed in Fig. 4(c), although they are still there. We find that the first-order directional derivative $b'_r = \boldsymbol{k}_r \cdot \nabla b$ of a Dirac cone is very small in one direction (defined by an angle $\phi_{\boldsymbol{k}}$) and becomes very large in the corresponding orthogonal direction. Here $\boldsymbol{k}_r = [k_x \cos(\phi_{\boldsymbol{k}}), k_y \sin(\phi_{\boldsymbol{k}})]$ and $\phi_{\boldsymbol{k}} = \arctan(k_y/k_x)$. Therefore, the excitation of the deformed Dirac cone will result in the directional diffraction of the incident light beam and the prohibited diffraction in the corresponding orthogonal direction.

D. Non-Hermitian lattice modulation

Next we investigate the Lorentz-modulated non-Hermitian photonic graphene lattice. The real part of the lattice is the same as that in Fig. 4, so we do not show it again. In the

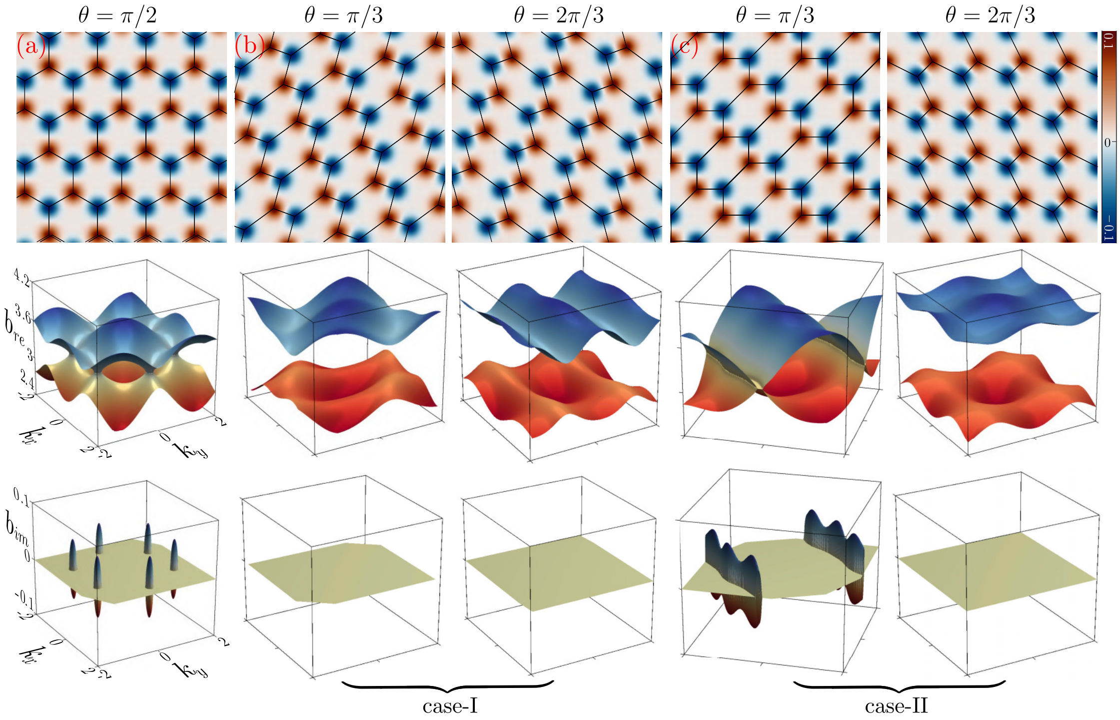

FIG. 5. Same as in Fig. 4 but for the non-Hermitian graphene lattice with $p_{\rm im} = 0.1$. Shown on top are the imaginary parts of the lattice, with red and blue representing the positive and negative values, respectively. Shown in the middle are the real parts of the band structure and on the bottom the corresponding imaginary parts of the band structure. The nonzero imaginary parts imply the existence of gain and loss in the lattice. Red and blue dots in the top row represent the lattice sites. The other parameters are the same as those in Fig. 4.

top panels in Fig. 5, we show only the imaginary part of the lattice. Since the Hamiltonian of the lattice is non-Hermitian, the corresponding eigenvalues are complex in general, except when the Hamiltonian meets the condition of $\mathcal{PT}$ symmetry. Hence, we separately show the real part b_{re} and the imaginary part b_{im} of the band structure in the middle and bottom panels of Fig. 5.

When the transformation angle is $\pi/2$, which corresponds to a regular photonic graphene lattice, there exist exceptional rings around the original Dirac points at the six corners of the first Brillouin zone in the real part of the band structure [28,43–48], as shown in Fig. 5(a). The imaginary part of the band structure, shown in the bottom panel of Fig. 5(a), indicates that the eigenvalues of the Hamiltonian of the system are indeed complex around the original Dirac points. The nonzero imaginary parts imply the existence of gain and loss at the lattice sites. However, if the complex lattice is $\mathcal{PT}$ symmetric, then the eigenvalues are completely real. Clearly, the non-Hermitian photonic graphene in Fig. 5(a) does not meet the condition of $\mathcal{PT}$ symmetry.

However, if the Lorentz transformation is introduced, the $\mathcal{PT}$ symmetry may be restored. In Fig. 5(b) we show the band structures of the case-I transformed photonic graphene lattice with two different angles. We find that the value of b_{im} is always zero throughout the first Brillouin zone (cf. the imaginary part of the band structure in the bottom panels), regardless of whether the transformation angle is larger or smaller than $\pi/2$. From this point of view, the non-Hermitian Hamiltonian of the system is $\mathcal{PT}$ symmetric, and the Lorentz transformation helps restore the $\mathcal{PT}$ symmetry. The reason for this result is that the transformation changes the symmetry of the lattice. We note that the conservative lattice in Fig. 4 gets deformed after the transformation, and the Dirac points move towards each other. For the non-Hermitian lattice, the exceptional rings move towards each other as well, but disappear if the deformation is large enough. In other words, the transformation operation restores the $\mathcal{PT}$ symmetry.

As concerns case II of the Lorentz-transformed photonic graphene lattice, depicted in Fig. 5(c), when the transformation angle θ is bigger than $\pi/2$ there is only the real part of the band structure and the $\mathcal{PT}$ symmetry is restored (cf. the column with $\theta = 2\pi/3$). If the angle is smaller than $\pi/2$, the $\mathcal{PT}$ symmetry cannot be restored (cf. the column with $\theta = \pi/3$). However, one cannot claim that this is a completely good outcome, because, as shown by the real part of the band structure with $\theta = \pi/3$, there are exceptional lines throughout the first Brillouin zone, which are distinct from the exceptional rings [44–48]. Considering that case III is a mirror image of case II, we obtain the $\mathcal{PT}$-symmetric transformed lattice in the region $\theta < \pi/2$ and the exceptional lines in the region $\theta > \pi/2$.

E. Movement trajectories of transformed Dirac points or exceptional rings

We track the movement of Dirac points with the transformation angle θ in the conservative lattice, as shown in Fig. 6. The results for the case-I lattice are exhibited in Fig. 6(a), in which the yellow dots represent Dirac points of the lattice without transformation (i.e., when the transformation angle is $\theta = 90^\circ$). We connect them by dashed lines to display the well-known hexagonal Brillouin zone. If the transformation angle θ decreases (increases) from $\theta = 90^\circ$, the Dirac points move in the direction indicated by the green (red) arrows. Regardless of whether the angle is decreased or increased, the Dirac points always coalesce, as indicated by the white dots. Numerical simulations demonstrate that the angle at which Dirac points coalesce is between 77° and 78° or between 102° and 103°. When the angle reaches 77° or 103°, the Dirac points disappear and band gaps appear in the band structure. The bottom two panels in Fig. 6(a) exhibit two examples of the band structure viewed from the top. The green dots and the red dots in these panels are the same as those in the top panel. For the case-II lattice, the movement of Dirac points is shown in Fig. 6(b). For this case, the Dirac points will not coalesce if the transformation angle θ is reduced from $\theta = 90^\circ$; see the trajectory indicated by the green arrows. Increasing the transformation angle from $\theta = 90^\circ$ leads to the coalescence of Dirac points, which happens between 100° and 101°. The bottom two panels in Fig. 6(b) display top views of the band structure at $\theta = 60^\circ$ and 100°, respectively, with the Dirac points highlighted with green and red dots.

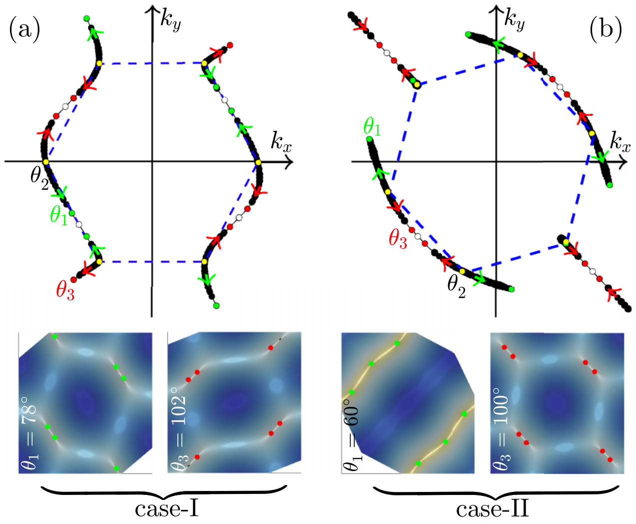

FIG. 6. Movement trajectories of Dirac points with the transformation angle θ in the Hermitian lattice. (a) Movement of six Dirac points in the case-I lattice. The yellow dots represent the six Dirac points of the honeycomb lattice without transformation (i.e., $\theta = 90^\circ$) that are connected by the dashed lines, which form the first Brillouin zone. The white dots mark the coalescence of Dirac points, while other dots are Dirac points with $\theta \neq 90^\circ$. The red arrows point to the movement of Dirac points with increasing θ from $\theta = 90^\circ$, while the green arrows are the same for the case with decreasing θ from $\theta = 90^\circ$. The bottom two panels show top views of the band structure corresponding to the angles indicated by the green and red dots. (b) Same as in (a) but for the case-II lattice. For this case, the coalescence of Dirac points happens only if $\theta > \pi/2$.

As concerns the non-Hermitian lattice, the $\mathcal{PT}$-symmetry condition is not fulfilled when $\theta = 90^\circ$. Therefore, there always exists an imaginary part in the band structure, shown by the bottom panel in Fig. 5(a). The larger the value of p_{im}, the broader the imaginary region in the band structure and the larger the exceptional rings. The results on the non-Hermitian

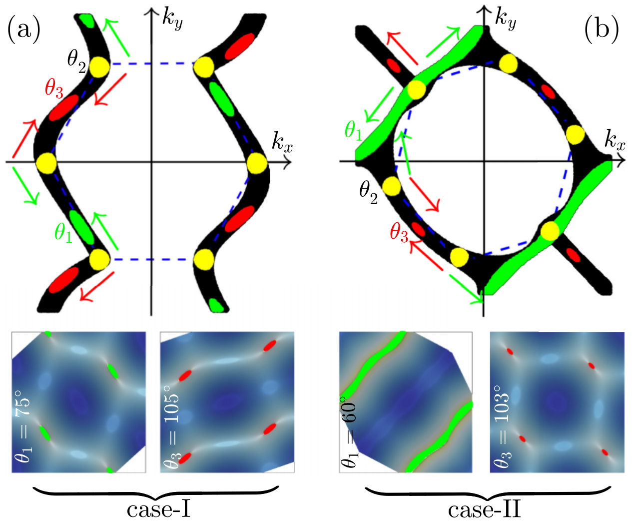

FIG. 7. Same as in Fig. 6 but for the non-Hermitian lattice with $p_{\text{im}} = 0.1$. The enclosed boundaries of the colored dots are exceptional rings.

case-I lattice are shown in Fig. 7(a). The yellow dots represent the exceptional rings with $\theta = 90°$, which move in the direction indicated by the red (green) arrows, when the transformation angle increases (decreases). This movement rule is similar to the conservative case in Fig. 6(a). However, the exceptional rings are easier to coalesce than Dirac cones. In the bottom panels of Fig. 7(a) we also show the top view of the band structures corresponding to the green and red coalesced exceptional rings in the top panel. Whenever the angle is further decreased or increased after the coalescence, the exceptional rings disappear and the $\mathcal{PT}$ symmetry of the non-Hermitian lattice is restored.

Now we turn to the non-Hermitian case-II lattice, as shown in Fig. 7(b). Recall that the Dirac points will not coalesce and disappear, as in the conservative counterpart [see the results in Fig. 6(b)]. Here the exceptional rings will coalesce but never disappear, even when the angle decreases, that is, the $\mathcal{PT}$ symmetry cannot be restored by reducing the transformation angle from $\theta = 90°$. However, since a coin has two sides, one obtains the exceptional lines from the coalesced exceptional rings, as shown by the green regions in Fig. 7(b). In contrast, if one increases the transformation angle from $\theta = 90°$, one may restore the $\mathcal{PT}$ symmetry. The two bottom panels show the exceptional rings (green stripes) and the coalesced exceptional rings about to disappear (red ellipses). Corresponding to the results in Figs. 6 and 7, the animations of movements with the transformation angle θ are also provided in [35], which clearly illustrate the movement trajectories.

III. CONCLUSION

In summary, the photonic graphene lattice modulated by a Lorentz-like transformation was investigated in detail, based on the continuous model. We classified the transformed lattice into two categories, cases I and II. For Hermitian lattices, Dirac cones will disappear for the case-I deformed lattices if $\theta \neq \pi/2$, while for case II, Dirac cones still exist if $\theta < \pi/2$ but are greatly deformed, which can be utilized for directional radiation. For non-Hermitian lattices, the Lorentz transformation can always restore the $\mathcal{PT}$ symmetry for the case-I lattices, but only under the condition $\theta > \pi/2$ for the case-II lattices. If $\theta < \pi/2$, exceptional lines may appear in the real part of the band structure throughout the first Brillouin zone. These results not only provide a new method for manipulating photonic lattices and restoring $\mathcal{PT}$ symmetry, but also may spark new ideas in both topological physics and non-Hermitian physics.

ACKNOWLEDGMENTS

This work was supported by the Natural Science Basic Research Program of Shaanxi Province (Program No. 2024JC-JCQN-06) of the National Natural Science Foundation of China (Grant No. 12474337).

DATA AVAILABILITY

The data that support the findings of this article are not publicly available. The data are available from the authors upon reasonable request.

---

[1] L. Lu, J. D. Joannopoulos, and M. Soljačić, Topological photonics, Nat. Photonics **8**, 821 (2014).

[2] T. Ozawa, H. M. Price, A. Amo, N. Goldman, M. Hafezi, L. Lu, M. C. Rechtsman, D. Schuster, J. Simon, O. Zilberberg, and I. Carusotto, Topological photonics, Rev. Mod. Phys. **91**, 015006 (2019).

[3] D. Smirnova, D. Leykam, Y. Chong, and Y. Kivshar, Nonlinear topological photonics, Appl. Phys. Rev. **7**, 021306 (2020).

[4] M. Segev and M. A. Bandres, Topological photonics: Where do we go from here? Nanophotonics **10**, 425 (2021).

[5] X. Zhang, F. Zangeneh-Nejad, Z.-G. Chen, M.-H. Lu, and J. Christensen, A second wave of topological phenomena in photonics and acoustics, Nature (London) **618**, 687 (2023).

[6] W. Yan, B. Zhang, and F. Chen, Photonic topological insulators in femtosecond laser direct-written waveguides, npj Nanophotonics **1**, 40 (2024).

[7] J. Noh, S. Huang, K. P. Chen, and M. C. Rechtsman, Observation of photonic topological valley Hall edge states, Phys. Rev. Lett. **120**, 063902 (2018).

[8] H. Zhong, S. Xia, Y. Zhang, Y. Li, D. Song, C. Liu, and Z. Chen, Nonlinear topological valley Hall edge states arising from type-II Dirac cones, Adv. Photonics **3**, 056001 (2021).

[9] Q. Tang, B. Ren, V. O. Kompanets, Y. V. Kartashov, Y. Li, and Y. Zhang, Valley Hall edge solitons in a photonic graphene, Opt. Express **29**, 39755 (2021).

[10] B. Ren, H. Wang, V. O. Kompanets, Y. V. Kartashov, Y. Li, and Y. Zhang, Dark topological valley Hall edge solitons, Nanophotonics **10**, 3559 (2021).

[11] M. C. Rechtsman, J. M. Zeuner, Y. Plotnik, Y. Lumer, D. Podolsky, F. Dreisow, S. Nolte, M. Segev, and A. Szameit, Photonic Floquet topological insulators, Nature (London) **496**, 196 (2013).

[12] S. Mukherjee, A. Spracklen, M. Valiente, E. Andersson, P. Öhberg, N. Goldman, and R. R. Thomson, Experimental observation of anomalous topological edge modes in a slowly driven photonic lattice, Nat. Commun. **8**, 13918 (2017).

[13] L. J. Maczewsky, J. M. Zeuner, S. Nolte, and A. Szameit, Observation of photonic anomalous Floquet topological insulators, Nat. Commun. **8**, 13756 (2017).

[14] S. K. Ivanov, Y. Q. Zhang, Y. V. Kartashov, and D. V. Skryabin, Floquet topological insulator laser, APL Photonics **4**, 126101 (2019).

[15] S. Mukherjee and M. C. Rechtsman, Observation of Floquet solitons in a topological bandgap, Science **368**, 856 (2020).

[16] L. J. Maczewsky, M. Heinrich, M. Kremer, S. K. Ivanov, M. Ehrhardt, F. Martinez, Y. V. Kartashov, V. V. Konotop, L. Torner, D. Bauer, and A. Szameit, Nonlinearity-induced photonic topological insulator, Science **370**, 701 (2020).

[17] T. Biesenthal, L. J. Maczewsky, Z. Yang, M. Kremer, M. Segev, A. Szameit, and M. Heinrich, Fractal photonic topological insulators, Science **376**, 1114 (2022).

[18] A. A. Arkhipova, Y. Zhang, Y. V. Kartashov, S. A. Zhuravitskii, N. N. Skryabin, I. V. Dyakonov, A. A. Kalinkin, S. P. Kulik, V. O. Kompanets, S. V. Chekalin, and V. N. Zadkov, Observation of π solitons in oscillating waveguide arrays, Sci. Bull. **68**, 2017 (2023).

[19] B. Xie, H.-X. Wang, X. Zhang, P. Zhan, J.-H. Jiang, M. Lu, and Y. Chen, Higher-order band topology, Nat. Rev. Phys. **3**, 520 (2021).

[20] Z.-K. Lin, Q. Wang, Y. Liu, H. Xue, B. Zhang, Y. Chong, and J.-H. Jiang, Topological phenomena at defects in acoustic, photonic and solid-state lattices, Nat. Rev. Phys. **5**, 483 (2023).

[21] J. Noh, W. A. Benalcazar, S. Huang, M. J. Collins, K. P. Chen, T. L. Hughes, and M. C. Rechtsman, Topological protection of photonic mid-gap defect modes, Nat. Photonics **12**, 408 (2018).

[22] Y. Liu, S. Leung, F.-F. Li, Z.-K. Lin, X. Tao, Y. Poo, and J.-H. Jiang, Bulk-disclination correspondence in topological crystalline insulators, Nature (London) **589**, 381 (2021).

[23] B. Ren, A. A. Arkhipova, Y. Zhang, Y. V. Kartashov, H. Wang, S. A. Zhuravitskii, N. N. Skryabin, I. V. Dyakonov, A. A. Kalinkin, S. P. Kulik, V. O. Kompanets, S. V. Chekalin, and V. N. Zadkov, Observation of nonlinear disclination states, Light Sci. Appl. **12**, 194 (2023).

[24] H. Zhong, V. O. Kompanets, Y. Zhang, Y. V. Kartashov, M. Cao, Y. Li, S. A. Zhuravitskii, N. N. Skryabin, I. V. Dyakonov, A. A. Kalinkin, S. P. Kulik, S. V. Chekalin, and V. N. Zadkov, Observation of nonlinear fractal higher order topological insulator, Light Sci. Appl. **13**, 264 (2024).

[25] M. C. Rechtsman, J. M. Zeuner, A. Tünnermann, S. Nolte, M. Segev, and A. Szameit, Strain-induced pseudomagnetic field and photonic Landau levels in dielectric structures, Nat. Photonics **7**, 153 (2013).

[26] Z. Yang, F. Gao, Y. Yang, and B. Zhang, Strain-induced gauge field and Landau levels in acoustic structures, Phys. Rev. Lett. **118**, 194301 (2017).

[27] B. Ren, H. Wang, M. R. Belić, Y. Li, X. Zhu, and Y. Zhang, Zero-energy edge states and solitons in strained photonic graphene, Phys. Rev. A **107**, 043504 (2023).

[28] A. Szameit, M. C. Rechtsman, O. Bahat-Treidel, and M. Segev, $\mathcal{PT}$-symmetry in honeycomb photonic lattices, Phys. Rev. A **84**, 021806(R) (2011).

[29] V. V. Konotop, J. Yang, and D. A. Zezyulin, Nonlinear waves in $\mathcal{PT}$-symmetric systems, Rev. Mod. Phys. **88**, 035002 (2016).

[30] R. El-Ganainy, K. G. Makris, M. Khajavikhan, Z. H. Musslimani, S. Rotter, and D. N. Christodoulides, Non-Hermitian physics and PT symmetry, Nat. Phys. **14**, 11 (2018).

[31] Y. Ashida, Z. Gong, and M. Ueda, Non-Hermitian physics, Adv. Phys. **69**, 249 (2020).

[32] J. D. Jackson, *Classical Electrodynamics*, 3rd ed. (Wiley, Hoboken, 1998).

[33] T. J. Eichelkraut, G. A. Siviloglou, I. M. Besieris, and D. N. Christodoulides, Oblique Airy wave packets in bidispersive optical media, Opt. Lett. **35**, 3655 (2010).

[34] Y. Zhang, M. R. Belić, H. Zheng, Z. Wu, Y. Li, K. Lu, and Y. Zhang, Fresnel diffraction patterns as accelerating beams, Europhys. Lett. **104**, 34007 (2013).

[35] See Supplemental Material at http://link.aps.org/supplemental/10.1103/PhysRevA.111.043526 for the animations of the Brillouin zones changing with the transformation angle θ corresponding to Fig. 3, as well as the movement rule of the Dirac points and exceptional rings corresponding to Figs. 6 and 7.

[36] M. S. Kirsch, Y. Zhang, M. Kremer, L. J. Maczewsky, S. K. Ivanov, Y. V. Kartashov, L. Torner, D. Bauer, A. Szameit, and M. Heinrich, Nonlinear second-order photonic topological insulators, Nat. Phys. **17**, 995 (2021).

[37] S. Shen, Y. V. Kartashov, Y. Li, M. Cao, and Y. Zhang, π mode lasing in the non-Hermitian Floquet topological system, APL Photonics **9**, 086113 (2024).

[38] H. Zhong, D. Mihalache, S. Shen, and Y. Zhang, The band structure of helical waveguide arrays in topological photonics: A tutorial, Rom. Rep. Phys. **76**, 903 (2024).

[39] Y. V. Kartashov and D. V. Skryabin, Two-dimensional topological polariton laser, Phys. Rev. Lett. **122**, 083902 (2019).

[40] H. Zhong, R. Wang, M. R. Belić, Y. Zhang, and Y. Zhang, Asymmetric conical diffraction in dislocated edge-centered square lattices, Opt. Express **27**, 6300 (2019).

[41] Y. Kang, H. Zhong, M. R. Belić, Y. Tian, K. Jin, Y. Zhang, F. Li, and Y. Zhang, Conical diffraction from approximate dirac cone states in a superhoneycomb lattice, Ann. Phys. (Berlin) **531**, 1900295 (2019).

[42] S. Shen, Y. Zhang, Y. V. Kartashov, Y. Li, and V. V. Konotop, Two-dimensional flat-band solitons in superhoneycomb lattices, Nanophotonics **13**, 4047 (2024).

[43] B. Zhen, C. W. Hsu, Y. Igarashi, L. Lu, I. Kaminer, A. Pick, S. L. Chua, J. D. Joannopoulos, and M. Soljačić, Spawning rings of exceptional points out of Dirac cones, Nature (London) **525**, 354 (2015).

[44] M. Parto, Y. G. N. Liu, B. Bahari, M. Khajavikhan, and D. N. Christodoulides, Non-Hermitian and topological photonics: optics at an exceptional point, Nanophotonics **10**, 403 (2021).

[45] Q. Yan, B. Zhao, R. Zhou, R. Ma, Q. Lyu, S. Chu, X. Hu, and Q. Gong, Advances and applications on non-Hermitian topological photonics, Nanophotonics **12**, 2247 (2023).

[46] H. Nasari, G. G. Pyrialakos, D. N. Christodoulides, and M. Khajavikhan, Non-Hermitian topological photonics, Opt. Mater. Express **13**, 870 (2023).

[47] A. Li, H. Wei, M. Cotrufo, W. Chen, S. Mann, X. Ni, B. Xu, J. Chen, J. Wang, S. Fan, C.-W. Qiu, A. Alù, and L. Chen, Exceptional points and non-Hermitian photonics at the nanoscale, Nat. Nanotechnol. **18**, 706 (2023).

[48] Q. Wang and Y. D. Chong, Non-Hermitian photonic lattices: Tutorial, J. Opt. Soc. Am. B **40**, 1443 (2023).